Ceramics International 44 (2018) 18471–18477

Contents lists available at ScienceDirect

Ceramics International

journal homepage: www.elsevier.com/locate/ceramint

The impact of the crystal structure and morphology on the electrochemical performance for $CuFe_2O_4$ in sodium ion batteries

Xue Li[a], Peng Dong[a], Cheng Liu[a], Xiaohua Yu[a], Jinbao Zhao[c], Shigang Sun[c], Jiaming Liu[a,b,*], Yingjie Zhang[a,**]

[a] National and Local Joint Engineering Laboratory for Lithium-ion Batteries and Materials Preparation Technology, Key Laboratory of Advanced Battery Materials of Yunnan Province, Faculty of Metallurgical and Energy Engineering, Kunming University of Science and Technology, Kunming 650093, PR China
[b] School of Metallurgy and Chemistry Engineering, Jiangxi University of Science and Technology, Ganzhou 341000, PR China
[c] State Key Laboratory of Physical Chemistry of Solid Surfaces, Collaborative Innovation Center of Chemistry for Energy Materials, College of Chemistry and Chemical Engineering, Xiamen University, Xiamen 361005, PR China

ARTICLE INFO

Keywords:
Sodium-ion batteries
Anode materials
$CuFe_2O_4$
Crystal structure

ABSTRACT

The crystalline-controllable $CuFe_2O_4$ nanoparticles are successfully synthesized by a facile and scalable combustion method and investigated as anode materials for sodium ion batteries (SIBs). First-principles calculations are employed to confirm the phase transition temperature. The effects of reaction temperature on the phase composition, morphology and sodium storage properties of the products are innovatively investigated in detail. XRD data show that the phases of products varied from cubic to tetragonal types with the increased calcination temperature. The morphological results indicate that as the calcination temperature increases, the $CuFe_2O_4$ particle size gradually increases from nanoscale (~ 25 nm) to submicron-scale (larger than 200 nm). The $CuFe_2O_4$ obtained at 150 °C exhibits superior electrochemical performance in the electrochemical tests. After 80 cycles, the discharge capacity remains 331.0 mA h g^{-1}, showing a high capacity retention (79.8%). The excellent electrochemical performance is mainly due to the cubic structure and nanoscale size, which can stabilize the material structure and offer a large activity area, facilitate Na ion diffusion and ease volume expansion.

1. Introduction

Recently, sodium ion batteries (SIBs) have attracted considerable interest as a potential alternative to lithium ion batteries (LIBs) for large-scale electric storage applications, owing to the high natural abundance of sodium and the similar working mechanism of SIBs and LIBs [1–4]. Unfortunately, the Na ion is larger and heavier (radius 1.02 Å, mass 22.99 g mol^{-1}) than the Li ion (radius 0.59 Å, mass 6.94 g mol^{-1}), and most anode materials used for LIBs face the problems of inferior electrochemical performance or even complete electrochemical inactivity in SIBs [5,6]. Hence, development of effective host anode materials that possess remarkable specific capacity and stable cycling performance for SIBs is urgently desirable but remains a considerable challenge [7,8].

Metal oxides, especially Fe-based oxides with conversion reactions, have been considered one of the promising materials for SIB anode materials due to their high sodium storage capacity. The Na^+ de/insertion reaction in metal oxide anode can be summarized as follows [9]:

$$MO + 2Na^+ + 2e^- \leftrightarrow M + Na_2O \quad (1)$$

where M is metal. Zhang et al. reported the sodium storage property of α-Fe_2O_3/rGO composites, which could deliver a capacity of 310 mA h g^{-1} at 100 mA g^{-1} after 150 cycles [10]. Kumar et al. fabricated Fe_3O_4 nanoparticles, and the discharge capacity after 50 cycles was 248 mA h g^{-1} at a current density of 83 mA g^{-1} [11]. Fe-based binary oxides, which can be regarded as the combination of Fe_2O_3 and other metal oxides, are considered to be attractive anode materials in LIBs because of their affordable price, natural abundance, chemical stability and high theoretical capacity [12–15], but they are scarcely reported as anode materials in SIBs. Kollu et al. fabricated $MnFe_2O_4$/rGO nanocomposites as anode materials for LIBs and SIBs via the co-precipitation method, which demonstrated a reversible capacity of

* Corresponding author at: National and Local Joint Engineering Laboratory for Lithium-ion Batteries and Materials Preparation Technology, Key Laboratory of Advanced Battery Materials of Yunnan Province, Faculty of Metallurgical and Energy Engineering, Kunming University of Science and Technology, Kunming 650093, PR China.
** Corresponding author.
E-mail addresses: 438616074@qq.com (J. Liu), 747648515@qq.com (Y. Zhang).

https://doi.org/10.1016/j.ceramint.2018.07.066
Received 16 June 2018; Received in revised form 7 July 2018; Accepted 7 July 2018
Available online 09 July 2018

258 mA h g^{-1} for SIBs at 0.1 C after 30 cycles [16]. A reversible capacity of ~ 450 mA h g^{-1} after 50 cycles was achieved for the $NiFe_2O_4$/rGO composite prepared by the one-step hydrothermal method as SIB anode materials [17]. $MgFe_2O_4$@C nanofibres obtained by an electrospinning technique exhibited a high rate capability and an ultra-long cycle life [18]. Rod-like $CuFe_2O_4$ was also synthesized through the coprecipitation method and delivered a discharge capacity of 281 mA h g^{-1} after 20 cycles at a current rate of 100 mA g^{-1} [19]. In these cases, a long reaction time, complicated operation or special instrumentation is indispensable.

In this work, for the first time, we report the fabrication of $CuFe_2O_4$ particles for use as SIB anode materials through solution combustion synthesis, which is a facile procedure with few time and energy requirements. $CuFe_2O_4$ particles of various crystal structures and morphologies were obtained through heat treatment at different temperatures. The impact of crystal structures and morphologies on electrochemical performance was studied in detail. The theoretical phase transition temperature was confirmed via first-principles calculations. The $CuFe_2O_4$ obtained at 150 °C exhibits the best sodium storage ability, with a reversible capacity of 331.0 mA h g^{-1} and a high capacity retention of 79.8% after 80 cycles.

2. Experimental

2.1. Synthesis of $CuFe_2O_4$ particles

The schematic illustration for the synthetic process of $CuFe_2O_4$ particles is shown in Fig. 1. It is a two-step synthesis process, consisting of solution combustion synthesis followed by a heat treatment. In a typical synthesis, 10 mmol of $Cu(NO_3)_2{\cdot}3H_2O$ (99%, Aldrich) and 20 mmol of $Fe(NO_3)_3{\cdot}9H_2O$ (99%, Aldrich) were dissolved in 70 mL deionized water. Then, 30 mmol of citric acid (99.5%, Aldrich), which acts both as the fuel and ligand, was added into the above solution. The mixture was continuously stirred for 5 min until the citric acid dissolved and a homogeneous solution was obtained. The resultant solution was heated at 90 °C with constant magnetic stirring for 7 h, transforming the solution into a xerogel. The xerogel was heated at 350 °C to undergo the auto-combustion progress and form the black precursor. Finally, the precursor was calcined in air at 500 °C for 2 h in the muffle furnace at a heating rate of 5 °C min^{-1}, and the precursors were also heated at 150 °C and 800 °C for 2 h for comparative studies (denoted as CuFe-150, CuFe-500 and CuFe-800, respectively).

2.2. Characterization

The as-prepared compounds were characterized by X-ray diffraction (XRD) using a Rigaku MiniFlex II X-ray diffractometer with Cu Kα radiation (λ = 0.154178 nm). First-principles calculations were performed using the Vienna ab initio simulation package (VASP) based on the density functional theory (DFT). The thermogravimetric-differential scanning calorimetry (TG-DSC) curve for the xerogel was recorded on a NETZSCH STA 449F3 in the range of 35–800 °C at a heating rate of 5 °C min^{-1} in air. Scanning electron microscope (SEM) micrographs were obtained on an FEI Nova NanoSEM 450 field emission scanning electron microscope. Transition electron microscope (TEM) images were obtained with a Tecnai G2 TF30 S-Twin transmission electron microscope.

2.3. Electrochemical measurements

Electrochemical performance was tested using a CR2016 coin cell assembled under Ar atmosphere with sodium metal as the counter electrode, a glass fibre as the separator, and a solution of 1 M $NaClO_4$ and 5 vol% fluoroethylene carbonate (FEC) in anhydrous propylene carbonate (PC) as the electrolyte. Working electrodes were prepared with the composition of 70 wt% $CuFe_2O_4$, 20 wt% conductive carbon blacks (super P) as a conductive additive and 10 wt% sodium carboxymethyl cellulose (CMC) binder. Galvanostatic charge-discharge cycling and rate performances of cells were performed in the range from 0.01 to 3.0 V (*vs.* Na/Na^+) with a Land BTI-40 (Wuhan, China) cell test system at room temperature. Cyclic voltammetry (CV) measurements were conducted at a scan rate of 0.1 mV s^{-1} in the voltage range of 0.005–3.0 V (*vs.* Na/Na^+) on a Metrohm Autolab PGSTAT302N (Netherlands). Electrochemical impedance spectroscopy (EIS) curves were also measured on a Metrohm Autolab PGSTAT302N over the frequency range of 0.01 Hz to 100 kHz.

3. Results and discussion

3.1. Structural and morphological characterization

Fig. 2a manifests the XRD patterns and the relevant structure models based on the crystal facet parameters for the copper ferrite samples heated at different temperatures. As seen, the calcination temperature significantly impacts the crystal structure of $CuFe_2O_4$. Peaks of CuFe-150 match well with those of cubic $CuFe_2O_4$ (PDF Card, No. 25-0283). However, the peaks of CuFe-800 can be indexed to tetragonal $CuFe_2O_4$ (PDF Card, No. 34-0425). In addition, CuFe-500 contains both characteristic cubic and tetragonal peaks. As the temperature increases, the peaks become sharper, which implies that crystallinity is improving and that the content of transition metal oxide impurities decreases as well.

The generalized gradient approximation (GGA) in the Perdew-Burke-Ernzerhof (PBE) parameterization for the exchange-correlation functional is used (Fig. 2b). We calculated the bulk structures of the metal oxides using a 5 × 5 × 5 Monkhorst-Pack k point mesh, and the

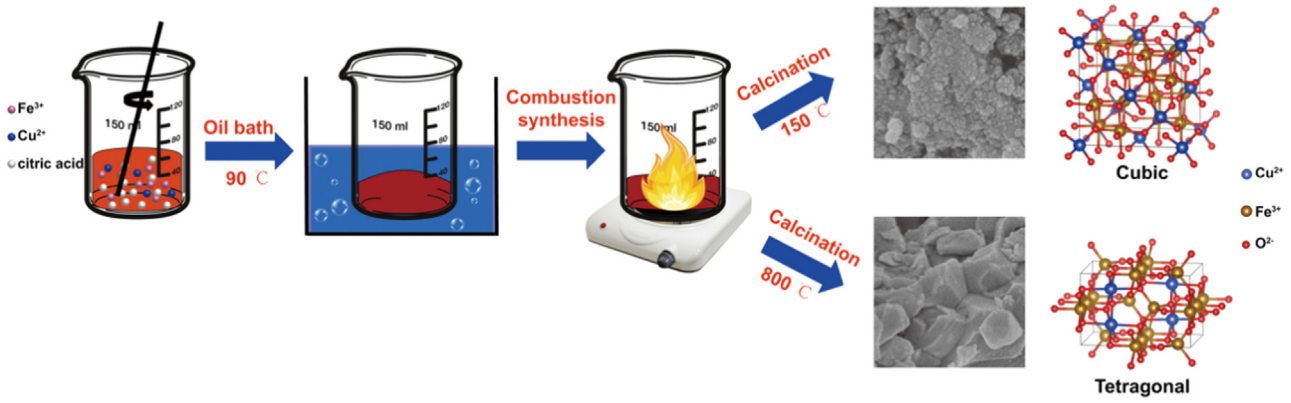

Fig. 1. Schematic illustration of the preparation process for $CuFe_2O_4$.

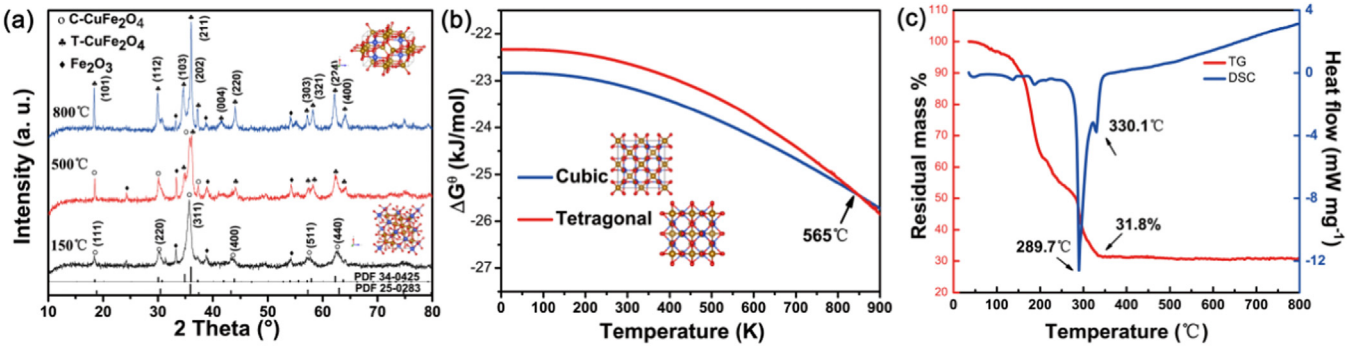

Fig. 2. (a) XRD patterns of the as-prepared samples. (b) The relationship plot between ΔG^{θ} and temperature for $CuFe_2O_4$. (c) TG-DSC curves of the xerogel.

energy cutoff was 500 eV. Here, we chose 5.0 and 4.0 eV as the U terms to describe Cu and Fe 3d states, respectively. The two types of structures of $CuFe_2O_4$ are shown in Fig. 2b. A 2 × 2 × 2 Supercell was built that shows partial occupation of Cu and Fe atoms. In the structure of $CuFe_2O_4$, the red, brown, and blue represent O, Fe, and Cu atoms, respectively. The relationship between ΔG^{θ} and temperature was calculated by the Phonopy-QHA method. From the curves in Fig. 2b, there is a large energy difference in ΔG^{θ} between cubic and tetragonal materials in the range of 0–500 °C. However, the energy difference decreases above 500 °C. There is an intersection at 565 °C, higher than 500 °C (the phase transition temperature in practice), which corresponds to the theoretical phase transition temperature. The differences in the phase transition temperatures between the experiment and simulation can be ascribed to the small size effect of nanomaterials. Nanomaterials possess small size effect, which can change nanomaterials' surface energy and gibbs free energy of phase transition process. Furthermore, phase transition temperature is concerned with atom binding energy, which decreases with the decrease of materials size [20,21]. The large particle size difference between CuFe-150 and CuFe-800 leads to the error of the simulation results.

The reaction process of the xerogel was examined by TG-DSC analysis (Fig. 2c). There are three apparent weight losses in the TG curve. The first weight loss occurred below 150 °C and could be attributed to the dehydration of absorbed water. Because of the massive reaction heat, a mass loss step and exothermic peak at 289.7 °C can be observed, which implies that the xerogel combusts at an autoignition temperature, and then a tiny mass loss step and exothermic peak at 330.1 °C indicate that the combustion reaction is approximately completed. The reaction is shown in Eq. (2). Eventually, the sample retains its mass residual rate at approximately 31.8% and maintains its heat absorption process at 350–800 °C. With regards to the XRD analysis results, they can be attributed to the crystal transfer process (from cubic to tetragonal crystal structures).

$$Cu(NO_3)_2 + 2Fe(No_3)_3 + \frac{20}{9}C_6H_8O_7 \frac{120}{9}CO_2 + \frac{80}{9}H_2O + 4N_2 + CuFe_2O_4 \quad (2)$$

FESEM characterization was carried out for morphological and structure analysis (Fig. 3). Fig. 3a reveals that the particle size of CuFe-150 is 15–35 nm. As Fig. 3b shows, the particle size of CuFe-500 is nonuniform; most are less than 30 nm, but a small number of particles are over 50 nm. In addition, the particle size of the sample calcined at 800 °C is clearly different from those of the other two samples in Fig. 3c. Most grain sizes of T-$CuFe_2O_4$ exceed 200 nm or even 500 nm. Submicron particles could reduce the material activity area, which will hinder the contact between the electrode, electrolyte and sodium storage during the charge/discharge processes. On the other hand, large particle size compresses the space between particles and are not beneficial for easing the volume change during the sodiation/desodiation processes. These factors may affect the electrochemical performances of T-$CuFe_2O_4$.

$CuFe_2O_4$ calcined at 150 °C and 800 °C was further characterized with TEM and HRTEM images. Fig. 4a and Fig. 4c show the difference in particle size between the two samples, and this is consistent with the observations from SEM. The HRTEM images of C-$CuFe_2O_4$ (Fig. 4b) reveal the lattice fringes with interplanar spacing (d) of 1.42 Å, corresponding to (440) planes, and d spacing of 2.09 Å for T-$CuFe_2O_4$ (Fig. 4d), corresponding to (220) planes.

3.2. Electrochemical performance

To investigate the electrochemical behaviour of $CuFe_2O_4$, cyclic voltammetry tests were employed, as shown in Fig. 5a–c. For all the samples, it is clear that the first cathodic scan is distinct from the subsequent cycles, especially for the sodiation process. As observed for CuFe-150 in Fig. 5a, there are three reduction peaks, located at 1.75, 1.04 and 0.01 V, during the first discharging process. Moreover, 1.75 V corresponds to the conversion reaction of CuO impurities [22]. A broad, irreversible peak reduction peak at 0.84 V is related to the organic electrolyte decomposition and a conversion of $CuFe_2O_4$ and Fe_2O_3 impurities, accompanied by the formation of an SEI film on the surface of the electrode [23–25]. The anodic peak at 0.77 V is attributed to the oxidation of Cu and Fe to CuO and Fe_2O_3, respectively, which is similar to the mechanism studied for LIBs [26,27]. In the subsequence cycles, the CV curves are very similar in shape and overlapped well, which indicates the good electrochemical reversibility and capacity retention of CuFe-150. Fig. 5c depicts CV curves of CuFe-800, which has few oxide impurities. There are only two reduction peaks located at 1.07 and 0.01 V, in the first cycle, and the anodic peak at 0.01 V is more intense than that of CuFe-150. In the subsequent sweeps, reduction and oxidation peaks shift to lower and higher potentials, respectively, indicating that the over-potentials are gradually increased and would hinder the energy conversion process and then reduce the power density. In addition, CuFe-500 has the characteristics of both CuFe-150 and CuFe-800, as shown in Fig. 5b.

Fig. 5d–f display the representative charge/discharge profiles of three samples in a potential range of 0.01–3.0 V (*vs.* Na/Na^+) at 50 mA g^{-1}. An apparent plateau from 0.2 V to 0.01 V in the initial discharge curves can be observed for the three samples, which can be attributed to the reduction of Cu^{2+} and Fe^{3+} to Cu^0 and Fe^0. The initial discharge and charge capacities of CuFe-150 are 652.7 and 422.3 mA h g^{-1}, respectively, with a coulombic efficiency of 64.7%. We did not observe significant capacity fading in the following charge/discharge processes, indicating excellent stability for CuFe-150. Charge/discharge capacities 503.2 and 721.3 mA h g^{-1} were obtained for CuFe-800 in the primary cycle, and a deep fall in the specific capacities, from the initial values to 342.3 and 349.0 mA h g^{-1}, respectively, were recorded after the 30th cycle. The enlarged views show that the polarization of CuFe-800 is more intense than that of the other two samples. This lower cyclic stability is consistent with the abovementioned CV results. The

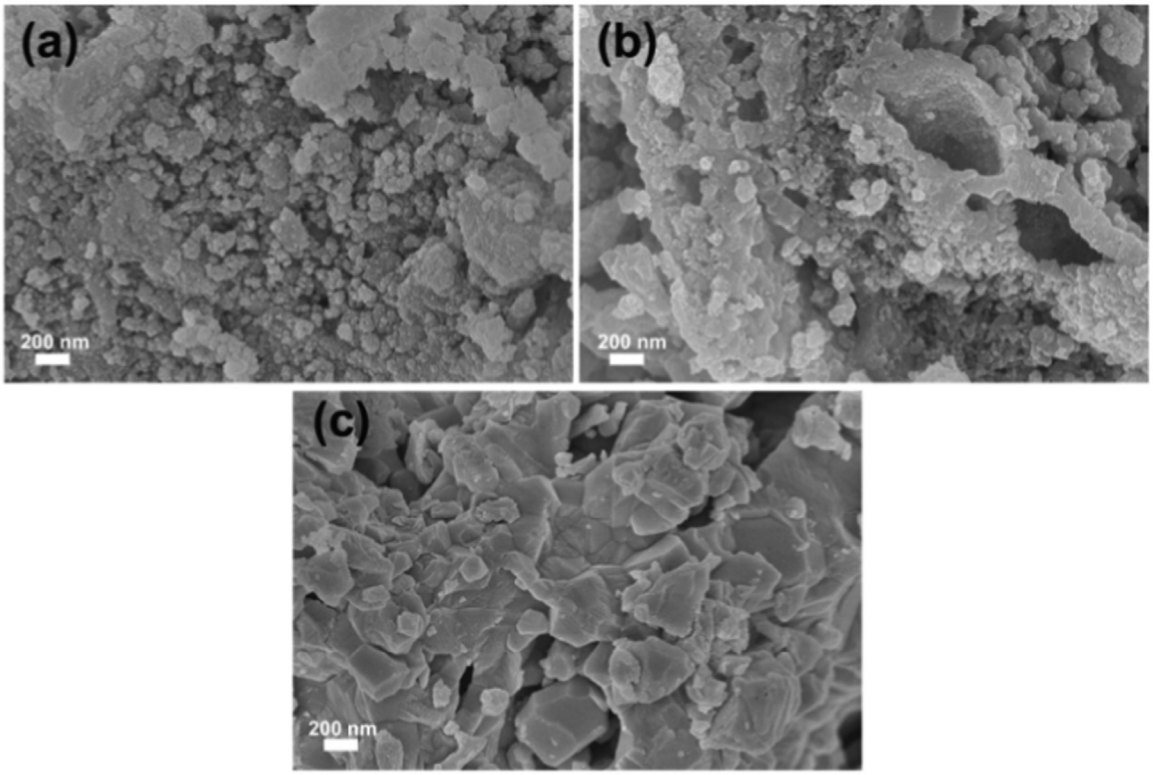

Fig. 3. FESEM images of (a) CuFe-150, (b) CuFe-500 and (c) CuFe-800.

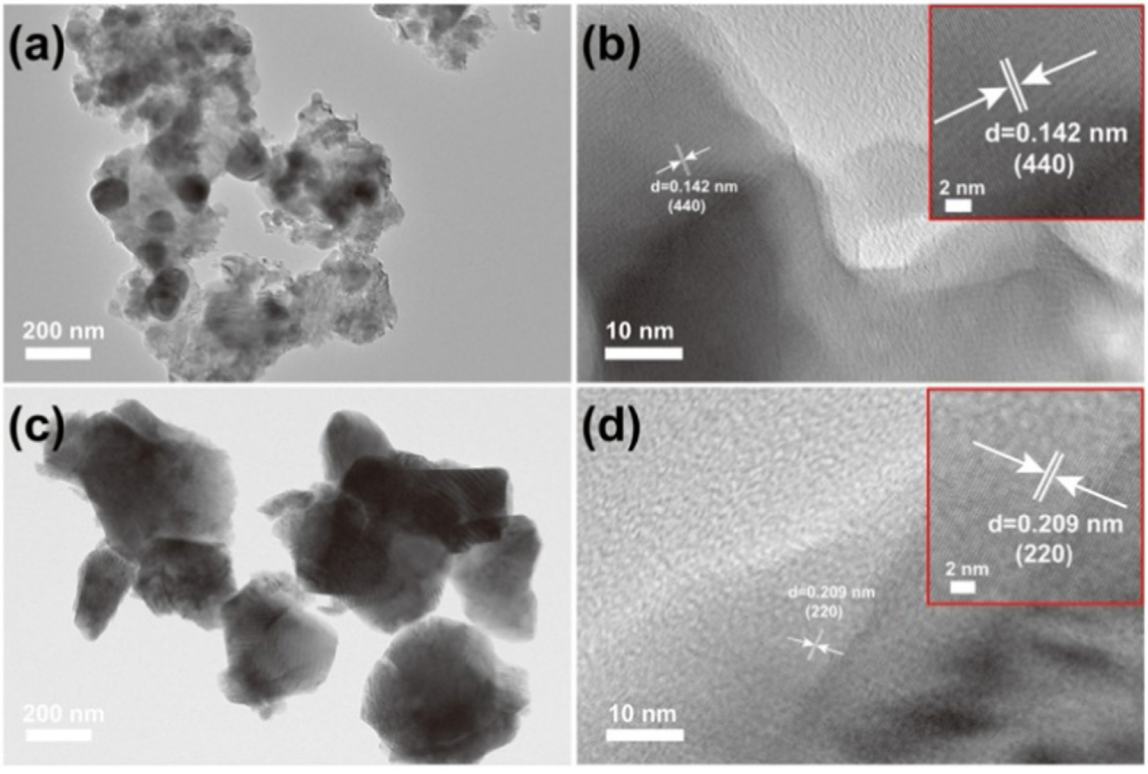

Fig. 4. TEM and HRTEM images of (a, b) CuFe-150 and (c, d) CuFe-800.

curves of CuFe-500 display a high stability and specific capacity (the discharge capacity can be maintained at 404.6 mA h g^{-1} in the 30th cycle), which is superior to that of CuFe-150 and CuFe-800.

Since the calcination temperature has a direct impact on the electrochemical properties of $CuFe_2O_4$, the cycling performances and rate capability of CuFe-150, CuFe-500 and CuFe-800 were further investigated from 0.01 to 3.0 V (*vs.* Na/Na^+). The cycling performances of the as-prepared samples and the coulombic efficiency of CuFe-150

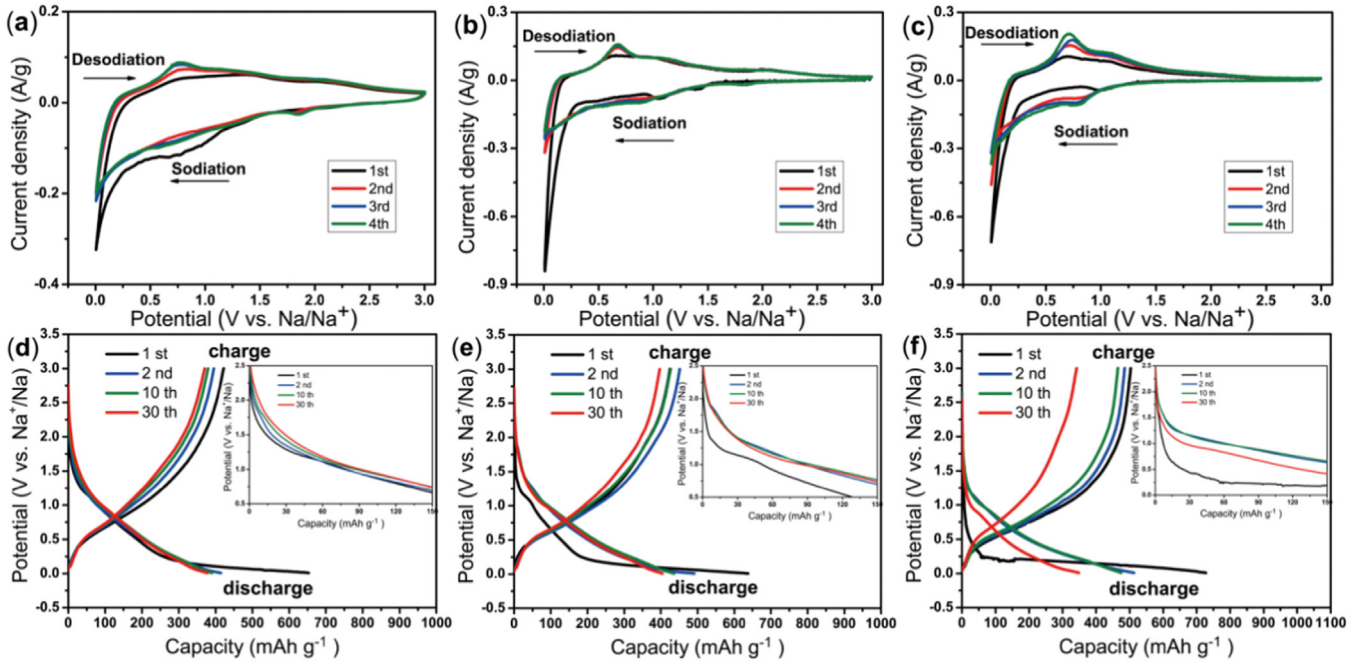

Fig. 5. Cyclic voltammetry plots of (a) CuFe-150, (b) CuFe-500 and (c) CuFe-800 for the first four cycles. Charge/discharge curves of (d) CuFe-150, (e) CuFe-500 and (f) CuFe-800 for the 1st, 2nd, 10th, and 30th cycle at 50 mA g^{-1}.

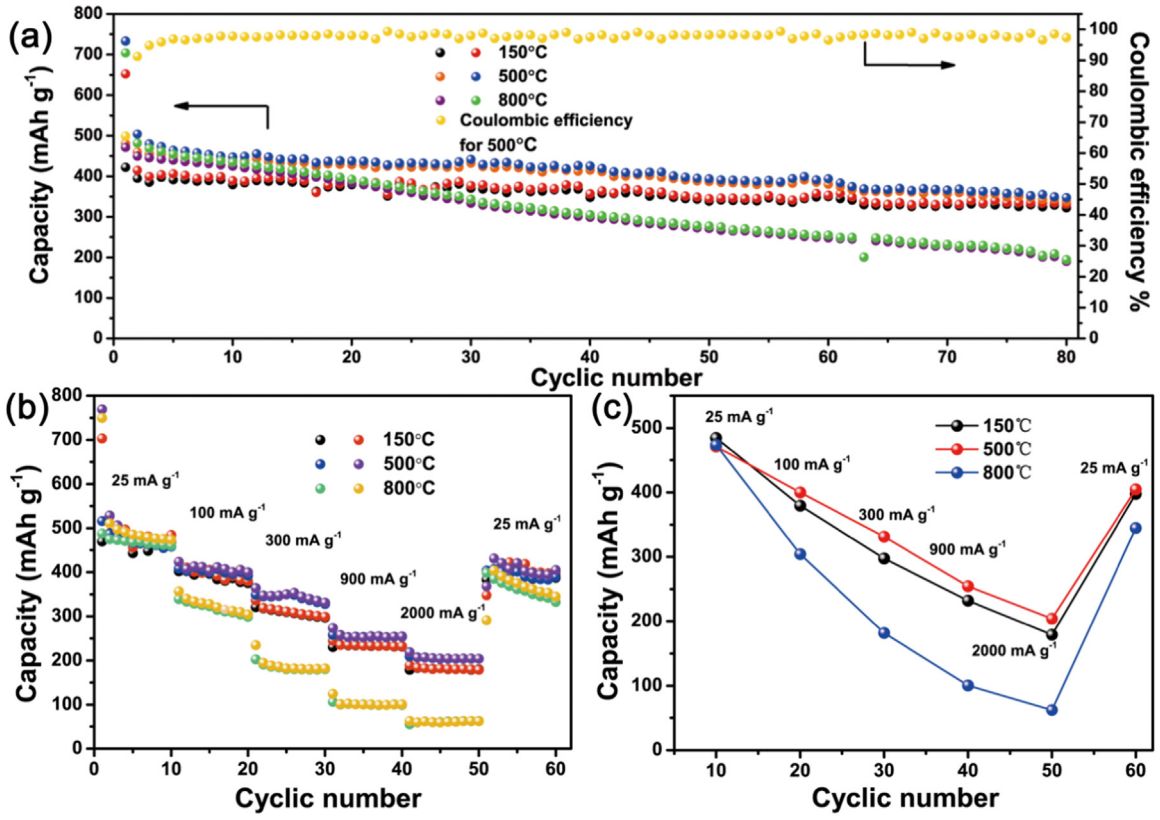

Fig. 6. (a) The cycling performance of CuFe-150, CuFe-500 and CuFe-800 at a current density of 50 mA g^{-1} (0.01–3.0 V). (b) Rate capabilities of CuFe-150, CuFe-500 and CuFe-800 electrodes at various current densities from 25 to 2000 mA g^{-1}. (c) Rate capability sketch of CuFe-150, CuFe-500 and CuFe-800.

with a current density of 50 mA g^{-1} are displayed in Fig. 6a. CuFe-500 exhibits a slightly higher specific capacity than that of CuFe-150 and CuFe-800 in the first 20 cycles. In the following cycles, the reversible capacity of CuFe-800 decays rapidly; however, CuFe-150 and CuFe-500 exhibit superior cycling stability. After 80 cycles, CuFe-500 delivers a discharge capacity of 347.3 mA h g^{-1}, higher than the 331.0 mA h g^{-1} of CuFe-150, while the capacity of CuFe-800 decreases to only 194.6 mA h g^{-1}. The above cycling performance test demonstrates that CuFe-800 exhibits dissatisfactory capacity retention. As shown in Table 1, there are some significant differences in crystallinity, crystal

Table 1
The differences between the as-prepared $CuFe_2O_4$ samples.

	Degree of crystallinity	Crystal structure	Size (nm)	The 80th cycle specific capacity (mA h g^{-1})	Capacity retention
CuFe-150	Worse	Cubic	15–35	331.0	79.8%
CuFe-500	Good	Cubic & tetragonal	30–80	347.3	68.8%
CuFe-800	Better	Tetragonal	> 200	194.6	40.5%

structure and particle size between the as-prepared $CuFe_2O_4$ samples. The capacity retention of the nanoscale CuFe-150, which is in a cubic structure, is 79.8%, which is almost 40% higher than that of the submicro-scale CuFe-800, which is in a tetragonal structure. This phenomenon may be caused by the native crystal structure and large particle sizes with a smaller active area that is not conducive for contact between the electrode and electrolyte and hinders lithium storage during the charge/discharge processes [28]. On the other hand, nanoscale particles can improve sodium diffusion due to the decrease of the diffusion path length, hence batteries show enhanced electrochemical property [29]. Furthermore, the higher crystallinity of CuFe-500 may result in better cycling performance than that of CuFe-150 [30].

In addition to the capacity and cycling stability, rate capability is another important property for batteries' applications. Fig. 6b and Fig. 6c depict the rate capabilities of the prepared sample electrodes under various current densities in the range of 25–2000 mA g^{-1}. In the initial ten cycles, all samples show a similar reversible capacity as high as approximately 475 mA h g^{-1}. Then, the current density is gradually increased to 100, 300, 900 and 2000 mA g^{-1}. The corresponding capacities of CuFe-500 can reach 400.1, 331.2, 254.5 and 203.9 mA h g^{-1}, respectively. When the rate returns to the initial 25 mA g^{-1}, the discharge capacity promptly recovers to 404.9 mA h g^{-1}. By contrast, CuFe-150 displays a slightly lower capacity. However, CuFe-800 exhibits an inferior rate performance. The discharge capacities obtained at 100, 300, 900 and 2000 mA g^{-1} are 304.2, 181.9, 100.6 and 62.1 mA h g^{-1}, respectively. The large CuFe-800 particles could not endure the stress caused by rapid Na ion insertion and extraction at a high current density. Particles may be pulverized in the charge/discharge processes, leading to a deterioration of the cyclability [31].

To further investigate the transport kinetics for the electrochemical properties of $CuFe_2O_4$ obtained at different calcination temperatures, electrochemical impedance spectroscopy (EIS) measurements were employed after 10 cycles. The Nyquist plots, which are composed of two depressed semicircles in high and medium frequencies followed by a slope line in the low frequency region, are shown in Fig. 7a. R_s indicates the ohmic resistance of the electrolyte, R_b is related to the small high frequency semicircle and denotes the SEI layer resistance, and the semicircle in the medium frequency region corresponds to R_{ct}, which represents the charge transfer resistance [16]. W is the Warburg impedance at low frequency and CPE represents the double-layer capacitance. The simulation results of the three samples are shown in Table 1. CuFe-150 exhibits the smallest R_{ct} and R_s values.

The diffusion coefficient of sodium ions could be evaluated according to EIS by using Eq. (3) [18,32]:

$$D_{Na} = 0.5\left(\frac{RT}{AFn^2C\sigma}\right)^2 \quad (3)$$

where R is the gas constant, T is the absolute temperature, A is the surface area of the electrode, n is the number of electrons per molecule during oxidization, F is the Faraday constant, C is the molar concentration of sodium ion and σ is the Warburg impedance coefficient, which relates to Z′ by Eq. (4) [18,33]. The σ values of $CuFe_2O_4$ samples can be obtained from the slope of Z′ vs. $\omega^{-1/2}$ plots, as presented in Fig. 7b.

$$Z' = R + \sigma\omega^{-1/2} \quad (4)$$

The σ values for three $CuFe_2O_4$ electrodes were calculated, and the results are shown in Table 2. As the calcination temperatures increases, σ values gradually increase. The value of CuFe-800 is largest, corresponding to the smallest D_{Na}. The result further demonstrates that large particle size is harmful to Na^+ ions' diffusion kinetics, leading to increased resistance.

4. Conclusion

In summary, various crystal forms and particle sizes of $CuFe_2O_4$ were successfully prepared through a feasible and efficient solution combustion synthesis method and used as anodes materials for SIBs. With the increased calcination temperature, the phases of products varied from cubic to tetragonal shapes, and particles sizes changed from nanoscale (~ 25 nm) to the submicron scale (larger than 200 nm). The results of first-principles calculations support the crystal structure transforming phenomenon, and the phase transition temperature is confirmed at approximately 565 °C. When being used as the anode materials for SIBs, CuFe-150 and CuFe-500 display improved specific capacity and cycling stability compared to CuFe-800. After 80 cycles, the reversible capacity of CuFe-150 and CuFe-500 anodes are close, corresponding to 330.1 and 347.3 mA h g^{-1}, respectively. However, the capacity retention of CuFe-150 is 11% higher than that of CuFe-500. This performance is due to the nano-sized particles (~ 25 nm) in a cubic structure, which could effectively buffer material volume expansion,

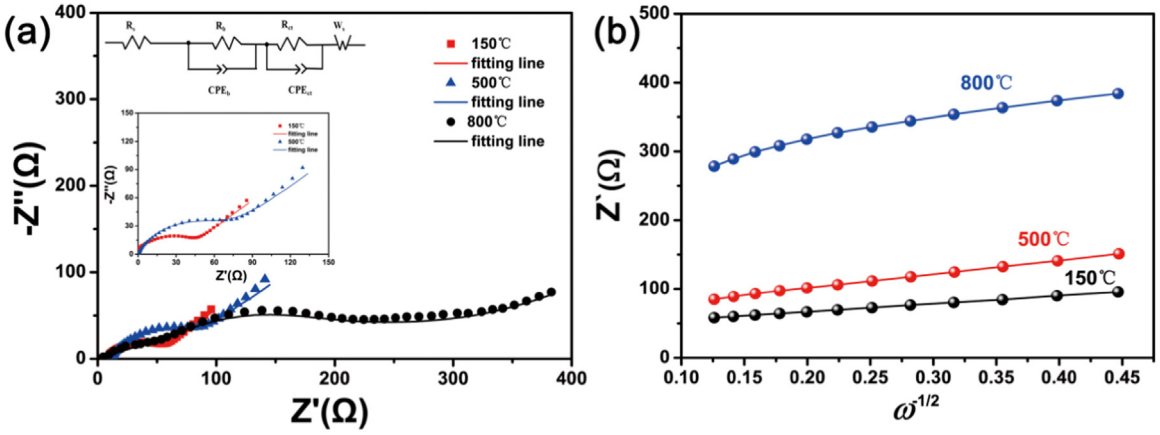

Fig. 7. (a) Nyquist plots of CuFe-150, CuFe-500 and CuFe-800 after 10 cycles, with an insert showing the electric equivalent circuit. (b) The relationship plot between Z' and $\omega^{-1/2}$ in the low-frequency region of $CuFe_2O_4$ samples.

Table 2
Simulated resistance values (R_b, R_{ct}), fitting errors and calculated Warburg factor (σ) of CuFe-150, CuFe-500 and CuFe-800.

	R_b (Ω)	R_{ct} (Ω)	Errors (%)	σ
CuFe-150	21.5	14.4	1.2	122.6
CuFe-500	139.1	50.7	2.4	260.9
CuFe-800	396.4	143.6	1.5	654.0

stabilize material structure, increase specific surface area and improve the Na^+ ions' diffusion kinetics. These merits make $CuFe_2O_4$ a prospective candidate as an anode material for applications in rechargeable SIBs. Moreover, the convenient and simple preparation of $CuFe_2O_4$ can be extended to the synthesis of other kinds of transition metal oxide electrode materials.

Acknowledgements

Financial support from National Natural Science Foundation of China (No. 51604132 and 51764029), Provincial Natural Science Foundation of Yunnan (No. 2017FB085) and the State Key Laboratory of Physical Chemistry of Solid Surfaces of Xiamen University (201506) are gratefully acknowledged.

References

[1] S.W. Kim, D.H. Seo, X. Ma, G. Ceder, K. Kang, Electrode materials for rechargeable sodium-ion batteries: potential alternatives to current lithium-ion batteries, Adv. Energy Mater. 2 (2012) 710–721.
[2] M.D. Slater, D. Kim, E. Lee, C.S. Johnson, Sodium-ion batteries, Adv. Funct. Mater. 23 (2013) 947–958.
[3] X. Zhang, M. Wang, G. Zhu, D. Li, D. Yan, Y. Lu, L. Pan, Porous cake-like TiO_2, derived from metal-organic frameworks as superior anode material for sodium ion batteries, Ceram. Int. 43 (2017) 2398–2402.
[4] Z. Li, J. Zhou, R. Xu, S. Liu, Y. Wang, L. Peng, W. Wu, M. Wu, Synthesis of three dimensional extended conjugated polyimide and application as sodium-ion battery anode, Chem. Eng. J. 287 (2016) 516–522.
[5] Y. Cao, L. Xiao, W. Wang, D. Choi, Z. Nie, J. Yu, L.V. Saraf, Z. Yang, J. Liu, Reversible sodium ion insertion in single crystalline manganese oxide nanowires with long cycle life, Adv. Mater. 23 (2011) 3155–3160.
[6] K. Tang, L. Fu, R.J. White, L. Yu, M.M. Titirici, M. Antonietti, J. Maier, Hollow carbon nanospheres with superior rate capability for sodium-based batteries, Adv. Energy Mater. 2 (2012) 873–877.
[7] S. Yang, W. Dong, D. Shen, S. Li, W. Sun, X. Hong, M. Wang, Y. Mao, Composite of nonexpansion reduced graphite oxide and carbon derived from pitch as anodes of Na-ion batteries with high coulombic efficiency, Chem. Eng. J. 309 (2016) 674–681.
[8] Q. He, S. Gu, T. Wu, S. Zhang, X. Ao, J. Yang, Z. Wen, Self-supported mesoporous $FeCo_2O_4$ nanosheets as high capacity anode material for sodium-ion battery, Chem. Eng. J. 330 (2017) 764–773.
[9] D. Li, D. Yan, J. Ma, W. Qin, X. Zhang, T. Lu, L. Pan, One-step microwave-assisted synthesis of Sb_2O_3/reduced graphene oxide composites as advanced anode materials for sodium-ion batteries, Ceram. Int. 42 (2016) 15634–15642.
[10] Z.J. Zhang, Y.X. Wang, S.L. Chou, H.J. Li, H.K. Liu, J.Z. Wang, Rapid synthesis of α-Fe_2O_3/rGO nanocomposites by microwave autoclave as superior anodes for sodium-ion batteries, J. Power Sources 280 (2015) 107–113.
[11] P.R. Kumar, Y.H. Jung, K.K. Bharathi, C.H. Lim, D.K. Kim, High capacity and low cost spinel Fe_3O_4 for the Na-ion battery negative electrode materials, Electrochim. Acta 146 (2014) 503–510.
[12] J. Cabana, L. Monconduit, D. Larcher, M.R. Palacín, Beyond intercalation-based Li-ion batteries: the state of the art and challenges of electrode materials reacting through conversion reactions, Adv. Mater. 22 (2010) E170–92.
[13] J. Haetge, C. Suchomski, T. Brezesinski, Ordered mesoporous MFe_2O_4 (M = Co, Cu, Mg, Ni, Zn) thin films with nanocrystalline walls, uniform 16 nm diameter pores and high thermal stability: template-directed synthesis and characterization of redox active trevorite, Inorg. Chem. 49 (2010) 11619–11626.
[14] W. Zhang, M. Li, Q. Wang, G. Chen, M. Kong, Z. Yang, M. Stephen, Hierarchical self-assembly of microscale cog-like superstructures for enhanced performance in lithium-ion batteries, Adv. Funct. Mater. 21 (2011) 3516–3523.
[15] S.F. Zheng, J.S. Hu, L.S. Zhong, W.G. Song, L.J. Wan, Y.G. Guo, Introducing dual functional CNT networks into CuO nanomicrospheres toward superior electrode materials for lithium-ion batteries, Chem. Mater. 20 (2008) 3617–3622.
[16] P. Kollu, K.P. Ramesh, S. Chella, D.K. Kim, A.N. Grace, High capacity $MnFe_2O_4$/rGO nanocomposite for Li and Na-ion battery applications, Rsc Adv. 5 (2015) 63304–63310.
[17] F. Wu, X. Wang, M. Li, H. Xu, A high capacity $NiFe_2O_4$/RGO nanocomposites as superior anode materials for sodium-ion batteries, Ceram. Int. 42 (2016) 16666–16670.
[18] Y. Liu, N. Zhang, C. Yu, L. Jiao, J. Chen, $MnFe_2O_4$@C nanofibers as high-performance anode for sodium-ion batteries, Nano Lett. 16 (2016) 3321–3328.
[19] X. Wu, W. Wu, Y. Li, F. Li, S. Liao, Synthesis and electrochemical performance of rod-like $CuFe_2O_4$ as an anode material for Na-ion battery, Mater. Lett. 138 (2015) 192–195.
[20] X. Jiang, M. Jiang, M. Zhao, Shape effect on the size and dimension dependent order-disorder transition temperatures of bimetallic alloys, Physica B 406 (2011) 4544–4546.
[21] Y. Li, W. Qi, Y. Li, E. Janssens, B. Huang, Modeling the size-dependent solid-solid phase transition temperature of Cu_2S nanosolids, J. Phys. Chem. C 116 (2012) 9800–9804.
[22] S. Yuan, X.L. Huang, D.L. Ma, H.G. Wang, F.Z. Meng, X.B. Zhang, Engraving copper foil to give large-scale binder-free porous CuO arrays for a high-performance sodium-ion battery anode, Adv. Mater. 26 (2014) 2273–2279.
[23] X. Zhang, W. Qin, D. Li, D. Yan, B. Hu, Z. Sun, L. Pan, Metal-organic framework derived porous CuO/Cu_2O composite hollow octahedrons as high performance anode materials for sodium ion batteries, Chem. Commun. 51 (2015) 16413–16416.
[24] X. Liu, T. Chen, H. Chu, L. Niu, Z. Sun, L. Pan, C.Q. Sun, Fe_2O_3-reduced graphene oxide composites synthesized via microwave-assisted method for sodium ion batteries, Electrochim. Acta 166 (2015) 12–16.
[25] B. Philippe, M. Valvo, F. Lindgren, H. Rensmo, K. Edström, Investigation of the electrode/electrolyte interface of Fe_2O_3 composite electrodes: Li vs Na batteries, Chem. Mater. 26 (2014) 5028–5041.
[26] R. Kalaiselvan, N. Kalaiselvi, C.O. Augustin, C.H. Doh, C. Sanjeeviraja, $CuFe_2O_4$/SnO_2 nanocomposites as anodes for Li-ion batteries, J. Power Sources 157 (2006) 522–527.
[27] L. Luo, R. Cui, H. Qiao, K. Chen, Y. Fei, D. Li, Z. Pang, K. Liu, Q. Wei, High lithium electroactivity of electrospun $CuFe_2O_4$ nanofibers as anode material for lithium-ion batteries, Electrochim. Acta 144 (2014) 85–91.
[28] N. Wang, H. Xu, L. Chen, X. Gu, J. Yang, Y. Qian, A general approach for MFe_2O_4 (M = Zn, Co, Ni) nanorods and their high performance as anode materials for lithium ion batteries, J. Power Sources 247 (2014) 163–169.
[29] S. Goriparti, E. Miele, F.D. Angelis, E.D. Fabrizio, R.P. Zaccaria, C. Capiglia, Review on recent progress of nanostructured anode materials for Li-ion batteries, J. Power Sources 257 (2014) 421–443.
[30] P. Lavela, J.L. Tirado, $CoFe_2O_4$ and $NiFe_2O_4$ synthesized by sol-gel procedures for their use as anode materials for Li ion batteries, J. Power Sources 172 (2007) 379–387.
[31] X. Wang, Y. Liu, Y. Wang, L. Jiao, CuO quantum dots embedded in carbon nanofibers as binder-free anode for sodium ion batteries with enhanced properties, Small 12 (2016) (4865-4776).
[32] X. Tang, X. Hou, L. Yao, S. Hu, L. Xiang, L. Xiang, Mn-doped $ZnFe_2O_4$ nanoparticles with enhanced performances as anode materials for lithium ion batteries, Mater. Res. Bull. 57 (2014) 127–134.
[33] N. Zhang, Z. Liu, T. Yang, C. Liao, Z. Wang, K. Sun, Facile preparation of nanocrystalline $Li_4Ti_5O_{12}$ and its high electrochemical performance as anode material for lithium-ion batteries, Electrochem. Commun. 13 (2011) 654–656.